A Passive Wireless Acceleration Sensing System Based on Patch Antenna and FMCW Radar

Zhuoran Yi, Liyu Xie, *Member, IEEE*, Songtao Xue, and Guochun Wan, *Member, IEEE*

***Abstract*—Traditional acceleration sensors use cables to transport data and batteries to supply power, which may increase failure risk, deployment inconvenience, and maintenance difficulty. This article proposes a passive and wireless acceleration sensing system, namely, a newly designed patch-antenna-based sensing node interrogated by frequency-modulated continuous-wave (FMCW) radar. The acceleration is correlated with the location of a cantilever beam, whose oscillation alters the additional capacitance of the patch antenna and consequently the resonant frequencies. The testing range can be adjusted by changing the material and dimensions of the cantilever beam, which is designed up to ±110 m/s^2 with a sampling rate of 500 Hz to meet the requirements of different conditions. The working mechanism of the sensing system is analyzed theoretically and then verified by the simulation in COMSOL Multiphysics. Then, an experiment is carried out to evaluate the performance of the sensing system. Both the resonant frequency and remaining power can be utilized to extract the acceleration response, and results show a good fit with the actual response (i.e., an average error of 4.5%). Empowered by FMCW Radar, the passive accelerometer may have great potential in identifying structure strain mode, impedance-based detection of bolt loosening, automation in construction, etc.**

***Index Terms*—Acceleration sensor, frequency-modulated continuous-wave (FMCW) radar, passive and wireless, patch antenna.**

I. INTRODUCTION

THE STRUCTURAL damages will accumulate with increased service time [1], [2]. To ensure structural capacity, it helps to acquire the safety index of the aged structure, such as strain, displacement, deflection, and acceleration [3], [4], [5]. Among these, acceleration is one of the most critical parameters for the dynamic analysis of vibration control [6], wind effect [7], stability of rotor motion [8], and earthquake monitoring [9], especially for super-high buildings [10] or long-span bridges [11].

Several wired sensors are proposed to detect structural acceleration, such as vibrating wire sensors [12], capacitance-type sensors [13], optical fiber sensors [14], and so on [15], [16]. These sensors are suitable for acceleration detection, with adequate accuracy, reliability, and detection range. However, due to the cables utilized for the power supply and data transmission, the line layout will be complex and labor-intensive due to the high cost of installation and troubleshooting [17].

To simplify the installation, experts have added some extra battery and communication units (such as Wi-Fi, ZigBee, and Bluetooth) into the sensor nodes to replace cumbersome cables [18], [19]. These accelerometers can achieve wireless detection, while a larger integrated sensing node is becoming a new problem. Besides, the excessive integration of the wireless sensing nodes will also enlarge the volume, decrease the reparability, and increase costs. Recently, it has been reported the application of a micrometer can reduce the volume. Several experts have proposed effective active wireless accelerators with smaller volumes according to microelectronic design [20], [21], [22]. Spencer et al. [23], Shajihan et al. [24], and Fu et al. [25] proposed a series of active wireless acceleration sensors and verified the workability according to the shaking table tests, bridges, and structures. However, the cost of these accelerometers is usually too high to apply in normal practice, especially when utilized in an underdeveloped area or for distributed sensing. Then, using a battery for the power supply will cause a potential environmental problem and will shorten the sensor's life [26], [27]. Besides, the reparability of these battery-powered accelerators is even worse compared with traditional active wireless accelerators.

Experts analyzed several passive wireless acceleration sensors to eliminate the influence of cable and battery. One idea is to use a mechanical ratcheting mechanism to obtain the accelerations [28], [29], [30]. The maximum displacement of embedded mass will be recorded and utilized to calculate acceleration. The acceleration can be obtained passively, while the real-time interrogation will be a problem. Besides, only the peak of acceleration is detected in this method. Another possible way is using a reflectometer as a monostatic radar for measuring vibration [31], [32], [33]. The phase change during S_{11} acquisition is calculated to reflect the target's vibration. This method can obtain acceleration passive-wirelessly, even without a sensing node. However, the surface of the target structure must be reflective (conductive), limiting the

---

Manuscript received 29 December 2022; accepted 23 January 2023. Date of publication 26 January 2023; date of current version 7 June 2023. This work was supported in part by the National Natural Science Foundation of China under Grant 52078375 and Grant 52178298, and in part by the Top Discipline Plan of Shanghai Universities—Class I. *(Corresponding author: Liyu Xie.)*

Zhuoran Yi and Liyu Xie are with the Department of Civil Engineering, Tongji University, Shanghai 200092, China (e-mail: yzr1997@tongji.edu.cn; liyuxie@tongji.edu.cn).

Songtao Xue is with the Department of Civil Engineering, Tongji University, Shanghai 200092, China, and also with the Department of Architecture, Tohoku Institute of Technology, Sendai 982-0831, Japan (e-mail: xue@tongji.edu.cn).

Guochun Wan is with the Department of Electronic Science and Technology, Tongji University, Shanghai 200092, China (e-mail: wanguochun@tongji.edu.cn).

Digital Object Identifier 10.1109/JIOT.2023.3240027

2327-4662 © 2023 IEEE. Personal use is permitted, but republication/redistribution requires IEEE permission.
See https://www.ieee.org/publications/rights/index.html for more information.

Authorized licensed use limited to: TONGJI UNIVERSITY. Downloaded on June 05,2023 at 01:44:33 UTC from IEEE Xplore. Restrictions apply.

practical utilization. A new kind of real-time passive wireless accelerometer suitable for all structures, with a simpler design and lower price, is expected in the future.

Antenna-based passive sensors provide a new alternative approach for improving wireless detection. The *S* parameters (usually resonant frequency) of the antenna are designed to be shifted according to the change of measurand. The changed *S* parameters will be obtained from the backscattering signal and analyzed using the targeted measurand. So, generally speaking, the antenna will act as the power supply and the sensing unit, which decreases the sensing node's complexity. At present, antenna sensors have been widely analyzed to achieve passive wireless detection of slow-changing parameters in the field of civil engineering, such as deformation [34], deflection [35], strain [36], temperature [37], and crack opening [38]. These antenna sensors can achieve passive and wireless sensing, but the deformation inside the antenna itself will introduce much error into the measurement due to the different types of glue and calibration, which enormously limits its utilization in practice. Instead of using a monolithic patch antenna, Wan et al. [17], Li et al. [39], Jiang et al. [40], and Xue et al. [41], [42] proposed several composed patch antenna sensors with additional parts to solve the problem. The sensing parameter is correlated with the relative displacement of the antenna's composed patch instead of the deformation of the monolithic patch. However, these sensors mainly use a vector network analyzer (VNA) for the interrogation, where the cable is still needed. In addition, not all of these sensors are capable of acceleration sensing due to the limitation of the VNA sampling rate. A wireless design for power harvesting and data transferring needs to be reconsidered.

Popular wireless power harvesting methods contain frequency-modulated continuous-wave (FMCW) radar [43], [44], [45], piezoelectric energy harvesters (PEHs) [46], self-capacitance-based wireless power transfer (WPT) [47], [48], [49], and so on [50], [51], [52]. Considering the signal of harvested antenna sensing node should be collected in the meantime, an FMCW radar is a potential interrogation method for the antenna sensor, since it has been clarified to be effective in harvesting and interrogating the sensing node simultaneously. Based on the FMCW radar, Yao et al. [53] proposed a reader with a high sampling rate. The interrogation signal is modulated on the carrier wave, so theoretically speaking, the sampling frequency can reach the modulation frequency of the carrier wave, up to 10 kHz, which is of a great potential in the vibration sensing field comparing with the other energy harvesting and signal interrogation methods.

This article presents a passive wireless acceleration sensing system made possible using FMCW radar for antenna interrogation. The sensing system consists of an acceleration sensing node and an FMCW interrogation radar. The sensing node has a patch antenna and a coupled parallel cantilevered patch above the radiation patch. An air gap of about 5 mm is set between the radiation patch and the cantilevered patch. The structural dynamic will shake the coupled parallel cantilevered patch, thereby oscillating the distance between the cantilevered patch and the radiation patch. This variation will cause a shift in the patch antenna's equivalent capacitance, resulting in a resonant frequency shift. Then, the resonant frequency and return loss will be extracted by the FMCW radar with a sampling frequency of about 500 Hz and utilized to investigate the displacement of the cantilevered patch. The acceleration of the patch is then obtained by its relationship with dynamic amplification. The authors first conducted an identification analysis using structural dynamics passively and wirelessly with a compact size and no energy cost. The combination of an antenna sensor and FMCW radar is expected to have a strong resistance to environmental noise, which can be easily extended to multiobject detection. As a passive wireless dynamic sensing method, it also provides a significant potential for other practical uses, such as impedance-based detection, identifying structural strain modes, and monitoring bolt loosening.

This article is organized as the following. Section II introduces the FMCW radar and sensing node relationship. The relationship between the remaining power, resonant frequency, and acceleration is calculated to show the sensing mechanism. In Section III, the parameters of the FMCW radar and sensing node are carefully designed to ensure a match with each other. A high-frequency structural simulator (HFSS) is applied in this section to verify the system workability. Section IV describes the sensing node fabrication and FMCW radar as well as the instrumentation setup of the experiments. The basic sensing system test is carried out in this section. Results are compared with the acceleration obtained by a slow-motion camera to verify the testing accuracy. Conclusions are then drawn, and future research potential is discussed.

II. METHODOLOGY

The acceleration sensing system consists of a sensing node, FMCW radar-based interrogation unit, and a data post-processing module. This sensing system process is described as follows: first, an oscillating voltage signal is generated by the FMCW radar and is translated into a plane wave by the emitting wideband antenna. This generated plane wave is then received by an antenna-based sensing node attached to the structure and transmitted to the receiving wideband antenna. The final signal is input to the post-processing part. The resonant frequency and return loss are then obtained from the minimum point of the backbone curve of the signal.

Since the displacement of the cantilevered patch will influence the resonant frequency and return loss by changing the equivalent capacitance, using these two parameters can calculate the dynamic displacement based on this relationship. After that, the acceleration is calculated based on the second derivative of the obtained dynamic displacement. A schematic of the sensing system is in Fig. 1, and the detailed methodology of each component will be discussed in this section.

A. FMCW and FMCW Radar

FMCW is a kind of continuous electromagnetic wave with repeated frequency change. In each repeated round, the FMCW frequency will linearly change from downlink to uplink, with the wave energy kept nearly constant. The time domain and frequency domain of a normal FMCW is shown

Authorized licensed use limited to: TONGJI UNIVERSITY. Downloaded on June 05,2023 at 01:44:33 UTC from IEEE Xplore. Restrictions apply.

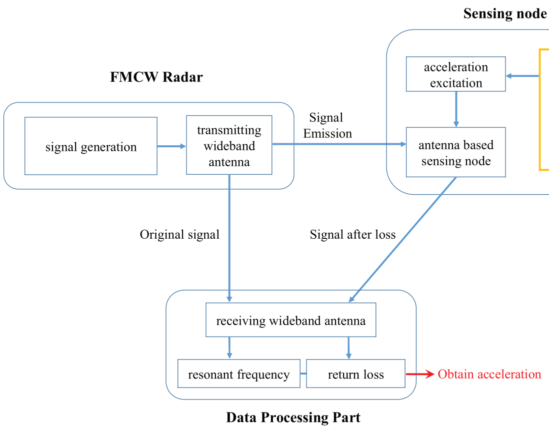

Fig. 1. Schematic of the sensing system.

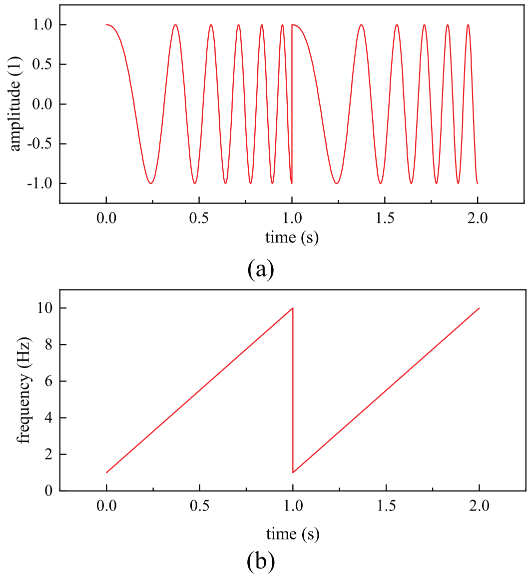

Fig. 2. Basic type of FMCW wave. (a) Time domain. (b) Frequency domain.

in Fig. 2. In this example, the downlink frequency is 1 Hz, the uplink frequency is 10 Hz, and the repetition frequency is 1 Hz.

Generally speaking, FMCW radar is a form of radar transmission and reception of an FMCW, wherein the transmitted signal's frequency is continuously varied at a known rate over a defined time period. A normal FMCW radar consists of a signal generation part and a signal transmission part. Fig. 3 shows the FMCW radar process in a one-way flowchart ending in emitting antenna transmission. The signal transmission part is usually a power amplifier and a transmitting wideband antenna. The basic signal is directly produced by a waveform generator. However, to interrogate the resonant frequency of the patch antenna, the working frequency of the FMCW radar needs to reach 5 GHz, which puts a demand on the frequency of the resonant source if directly produced by the waveform generator. To decrease this frequency requirement, a voltage-controlled oscillator (VCO) is used to boost the initial low-frequency voltage signal to a higher frequency.

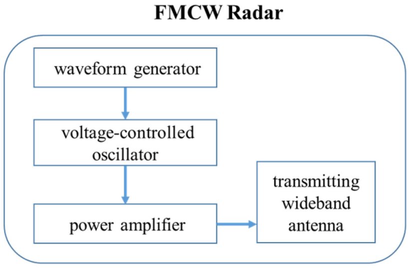

Fig. 3. FMCW radar process conception from waveform generation to wideband antenna transmission.

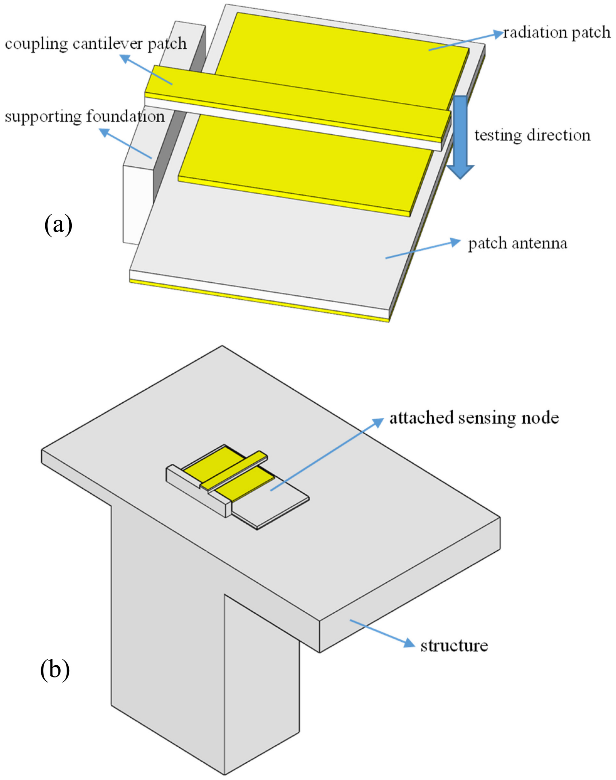

Fig. 4. Schematic of the sensing node. (a) Basic design. (b) Installation.

B. Sensing Node for the Detection of Acceleration

In the acceleration sensing system, the sensing node is used to change the acceleration signal of the structure to an electric signal and then transmit it as an electromagnetic signal. For this purpose, a traditional node should contain at least one power supply part for sensor activation, a signal sensing part for signal transformation, and a signal transmitting part for signal emission. A new patch antenna-based node with a coupled cantilevered patch unit is proposed, as displayed in Fig. 4(a). When it is attached to the vibrated structure, the coupled cantilevered patch will move up and down, corresponding to the shaking of the target building in the testing direction. Since the cantilevered patch can be regarded as a changeable capacitance to the bottom patch antenna, the S parameters will shift with the disturbance of the up-and-down movement of the cantilevered patch.

Fig. 5 illustrates the patch antenna sensing node designed to interrogate the wave where the dislocation of the upper patch

Authorized licensed use limited to: TONGJI UNIVERSITY. Downloaded on June 05,2023 at 01:44:33 UTC from IEEE Xplore. Restrictions apply.

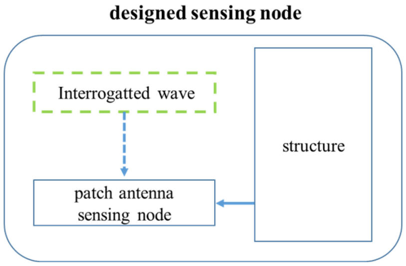

Fig. 5. Detailed conception of designed sensing node developed in this research.

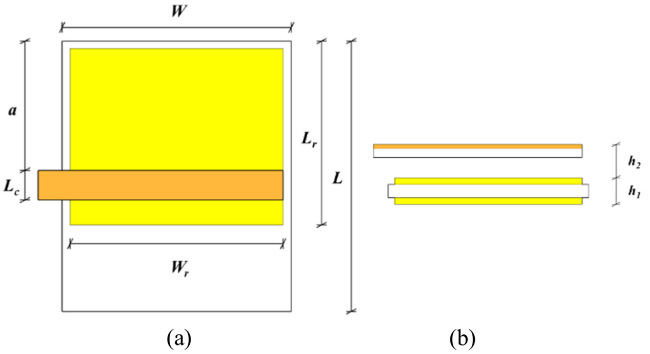

Fig. 6. Parameters of proposed sensing node. (a) Top view. (b) Side view.

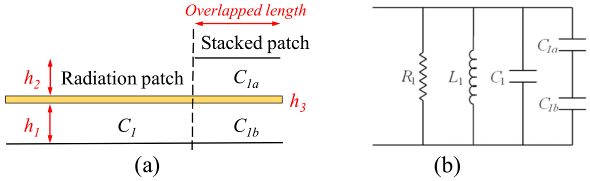

Fig. 7. Equivalent model. (a) Two-layer patch antenna. (b) Circuit model.

can be reflected by the S parameters of the bottom antenna. Then, the dislocation is regarded as the displacement under an equivalent dead load of the acceleration load. The acceleration of the target structure can then be obtained from the dynamics of the amplification relationship.

The dimension parameters of the antenna sensing node are provided in Fig. 6. W and L are the width and length of the bottom patch. W_r and L_r are the width and length of the radiation patch. These parameters decide the basic workability of the patch antenna. a and h_2 are the distance between the coupling cantilevered patch and the bottom patch antenna in the length and height direction. These two parameters determine the equivalent capacitance introduced by the cantilevered patch, which further controls the effectiveness rate of the cantilevered patch vibration to the bottom patch antenna to the S parameter. To further clarify the workability, resonant frequency, and return loss (S11). Equivalence capacitance was calculated theoretically based on these parameter settings.

Ignoring the effect of the supporting foundation, the sensing node is equivalent to a two-layer patch antenna [34], as shown in Fig. 7(a). Then, the parameter effects can be analyzed by the equivalent circuit model illustrated in Fig. 7(b) [34].

During the analysis, the inductance and resistance are regarded as approximately constant values. With the vibration of the cantilevered patch, the equivalent capacitance changed by further development toward the resonant frequency shift. Based on Xue's work [34], the resonant frequency f can be calculated as

$$f = \frac{1}{2\pi\sqrt{C_{be}L_1}} \tag{1}$$

where C_1 is the capacity of the uncovered area. C_{1a} and C_{1b} are the capacities of the covered area. L_1 is the inductance of the equivalent circuit. C_{be} is the equivalent capacity of C_1, C_{1a}, and C_{1b}, and can be defined as

$$C_{be} = C_1 + \frac{C_{1a}C_{1b}}{C_{1a}+C_{1b}} = \frac{W(L_{be}-L_{ov})\varepsilon}{h_1} + \frac{WL_{ov}\varepsilon}{h_1+h_2}. \tag{2}$$

Combining (1) and (2), the resonant frequency can be rewritten as

$$f \approx \frac{c\sqrt{L_{be}+(1-k)L_{ov}}}{2L_{be}\sqrt{\varepsilon L_{be}}} = G_1(h_2) \tag{3}$$

where L_{be} is the length of the radiation patch. L_{ov} is the overlapped length. ε is the dielectric constant of the substrate of the lower patch antenna. k is a height-related parameter, which is obtained from

$$k = h_1/(h_1+h_2) \tag{4}$$

where h_1 is the height of the substrate, and h_2 is the distance between the cantilevered patch and the radiation patch.

Then, the return loss S_{11} can be calculated as

$$S_{11} = -20\log\left(\frac{1}{|R|}\right) \tag{5}$$

where R is the voltage reflection coefficient defined as

$$R = \frac{(Z_{\text{in}}-Z_0)}{(Z_{\text{in}}+Z_0)} \tag{6}$$

where Z_{in} is the input independence, and Z_0 is the characteristic impedance defined as

$$Z_0 = \sqrt{\frac{L_1}{C_{be}}}. \tag{7}$$

Equation (2) shows that the equivalent capacity of C_{be} depends on the cantilevered patch location. If we assume the inductance and input independence will not change with the vibration of the cantilevered beam patch, the return loss will also be only determined by h_2, as follows:

$$S_{11} \approx -20\log\left(\frac{1}{\left|\frac{\left(Z_{\text{in}}-\sqrt{\frac{L_1}{C_{be}}}\right)}{\left(Z_{\text{in}}+\sqrt{\frac{L_1}{C_{be}}}\right)}\right|}\right) = G_2(h_2). \tag{8}$$

From (3) and (8), the patch antenna sensor's resonant frequency and return loss are determined by the distance between the stacked patch and the radiation patch h_2. When the patch antenna sensor is attached to a target structure, the distance, h_2, is related to the structural dynamics. Fig. 8 shows how the stacked patch can theoretically be considered

Authorized licensed use limited to: TONGJI UNIVERSITY. Downloaded on June 05,2023 at 01:44:33 UTC from IEEE Xplore. Restrictions apply.

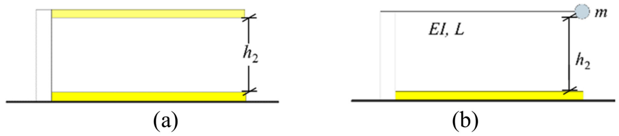

(a) (b)

Fig. 8. Equivalent beam. (a) Original and (b) equivalent single degree of freedom (SDOF) system.

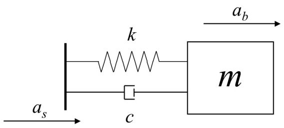

Fig. 9. Equivalent dynamic model for the sensing node.

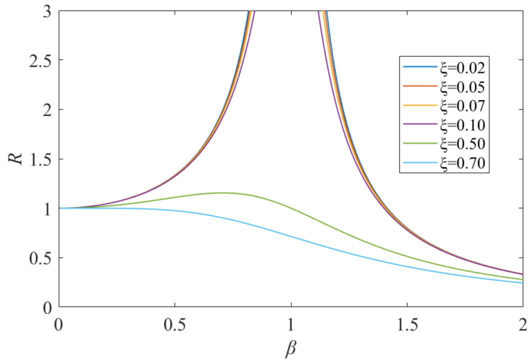

Fig. 10. Relationship between D, β, and ξ.

a cantilevered patch when the lower patch antenna is solidly connected to the target structure.

When the attached building experiences shaking, a corresponding vibration y will be experienced by the cantilevered patch, which can be simply calculated by solving

$$y = ma_b l^3/(3EI) \tag{9}$$

where m and a_b are the equivalent mass and acceleration of the beam. E and I are the beam's elasticity modulus and sectional inertia moment. Thus, (9) can be used to decide the testing range of acceleration.

Once the dimension size of the cantilevered patch is determined, the acceleration of the equivalent mass can only be related to the acceleration of the attached structure a_s.

The dynamic model for the sensing node is shown in Fig. 9, where m, k, and c are the equivalent mass, stiffness, and damping, respectively. Assuming two loading conditions for this model: the first loading condition involves a dead load mass on the mass, m, will cause a displacement, y_s, of the mass. The second loading condition is a dynamic acceleration, which results in a displacement, y, on the mass. Based on the previous analysis of the resonant reaction of a structure [54], the relationship between these two displacements can be described as

$$y = Dy_s, y_s = \frac{ma_s}{k} \tag{10}$$

where D is the dynamic amplification factor and can be calculated by

$$D = \left[\left(1-\beta^2\right)^2 + (2\xi\beta)^2\right]^{-0.5} \tag{11}$$

where ξ is the damping ratio. β is the frequency ratio of the beam and attached structure, which is defined as

$$\beta = \omega_c/\omega_s = \left(\pi^2\sqrt{\mathrm{EI}/\rho A}\right)/\left(L^2\omega_s\right) \tag{12}$$

where β is the frequency ratio of the beam and attached structure. ρ and A are the density and section area of the beam. ω_c and ω_s are the basic resonant frequencies of the beam and attached structure. Combining (10)–(12), the relationship between D, β, and ξ is displayed in Fig. 10.

Since the value of dynamic amplification factor D is nearly 1 when the frequency ratio β is limited to 0.2 from this figure, the displacement of the cantilevered patch y can be regarded as the static displacement y_s if the frequency ratio is well designed. Then, based on (10), the acceleration of the target structure can be finally obtained from this displacement, as

$$a_s = y_s k/m. \tag{13}$$

Then, after combining (3), (8), and (10), the relationship between the resonant frequency, return loss of the antenna sensor, and acceleration of structure a_s can be described as

$$f = G_1(h_2) = T_1(a_s) \tag{14}$$

$$S_{11} = G_2(h_2) = T_2(a_s). \tag{15}$$

C. Data Processing Part

This unit generates a designed FMCW wave and then transmits it to the sensing node. Then, the patch antenna sensor absorbs a part of the FMCW signal, causing a decrease in the FMCW radar power. The process of the power loss can be described in (16) and Fig. 11(a) as

$$P_{\text{in}} = P_b + P_l + P_r \tag{16}$$

where P_{in} is the input power of the FMCW frequency; P_b is the backscattering power transformed from FMCW radar to the antenna node, and P_r is the remaining power of the FMCW after interrogation of the sensing node. P_l is the loss of the remaining power (P_r) input.

When the FMCW frequency reaches the sensing node resonant point, the remaining power P_r will decrease to the lowest point since the power will be transmitted to the antenna sensing node as P_b to the maximum extent. Since the remaining power signal will not be caught by the receiving antenna due to the cross Ppolar isolation, the backscattering power signal P_b will then be detected by the receiving wideband antenna and further translated to a digital signal by the analog–digital converter (ADC). The whole progress is displayed in Fig. 11 for further clarification.

Based on this method, the resonant frequency of the antenna node can be obtained by analyzing the time during which the remaining power P_r reaches the lowest point. Since the return loss is hard to obtain during wireless detection, the remaining power is utilized to reflect the return loss. Due to propagation loss's influence, the remaining power can only be regarded as

Authorized licensed use limited to: TONGJI UNIVERSITY. Downloaded on June 05,2023 at 01:44:33 UTC from IEEE Xplore. Restrictions apply.

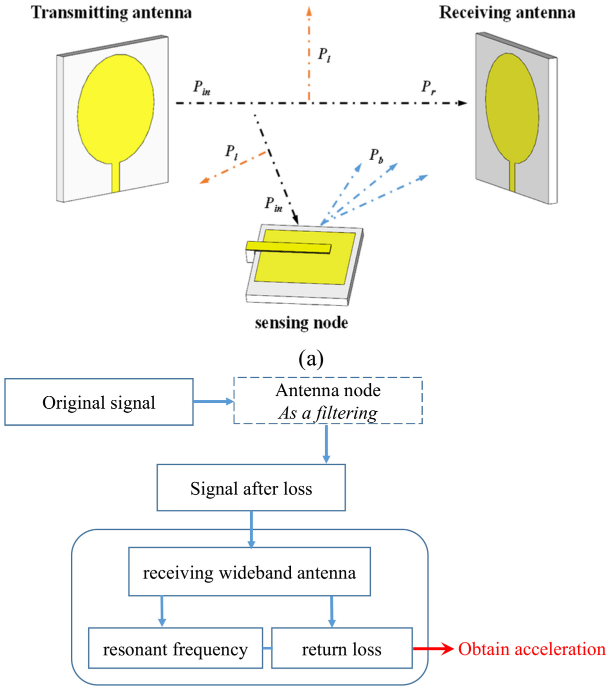

(a)

(b)

Fig. 11. Data processing diagrams. (a) Illustration of how the sensing node handles received power and how that power is transformed and used by transmitting and receiving antennas. (b) Flowchart of how each signal is handled and the results. The whole process provides a way to obtain an accurate assessment of the acceleration.

a relative property in practical use. Considering (14) and (15), the remaining power can be shown as

$$P_r = k_p S_{11} = k_p T_2(a_s) = k_p T_2\left(T_1^{-1}(f)\right) \tag{17}$$

where T_1^{-1} is the inverse function of T_1, k_p is the influence factor of the propagation loss and can be calculated by considering the resonant frequency of the first testing point or initial calibration point, which can be expressed as

$$k_p = P_r/T_2\left(T_1^{-1}(f)\right) \approx P_r(t_0)/T_2\left(T_1^{-1}(f(t_0))\right) \tag{18}$$

where t_0 corresponds to the initial time of the investigation.

That is, the acceleration of the targeting structure can be obtained by this method since these parameters and their relationship with each other were confirmed in Section II-B.

III. SIMULATION IN COMSOL MULTIPHYSICS®

The feasibility was confirmed in Section II. To determine the workability and corresponding parameters of the authors' newly designed patch antenna sensing node, a simulation based on COMSOL Multiphysics® ver. 6 was carried out. To simplify the simulation, only the workability of the sensing node is considered, and the FMCW radar used for interrogation is replaced by the lamb port as the feeding mechanism. The sweep frequency was set at 2.3 to 2.5 GHz, corresponding to the downlink frequency and uplink frequency of FMCW radar, respectively.

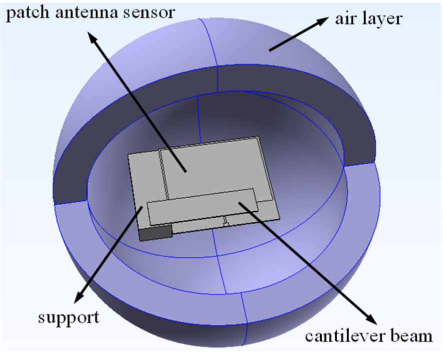

Fig. 12. Model in COMSOL Multiphysics®.

TABLE I
BASIC PARAMETERS OF THE SIMULATION SETTINGS

Parameters	**L** (mm)	**W** (mm)	**L_r** (mm)	**h_1** (mm)	**W_r**(mm)
Value	54.3	51	41.3	0.508	49
Parameters	**E** (MPa)	h_2 (mm)	a (mm)	L_c (mm)	
Value	1070	4	24	12	
Parameters	a_0 (m/s^2)	ω (1)	ρ (kg/m^3)	ξ (1)	
Value	50	2	2200	0.1	

A. Setup of Simulation in COMSOL Multiphysics®

Fig. 12 shows the model in COMSOL Multiphysics with the subtracting material and the cantilevered beam is constructed using the RT/duroid 5880 laminate to ensure the workability of the proposed antenna sensor. The boundary of the radiation patch and the upper surface of the cantilevered beam is assumed as Perfect E. The whole sensor is placed inside an airball set as a radiation boundary to consider the far-field effect. The lower surface of this sensor is fixed to simulate the condition when the sensor is attached to the structure. The antenna sensor was excited by a lumped port at the end of the feed line instead of plane wave excitation to simplify the simulation.

The antenna sensor was designed to work at around 2.45 GHz. Based on (1)–(4), the basic parameters and properties of the antenna sensor are initially determined and listed in Table I, where E is the Young Modulus of the cantilevered beam made with RT/duroid 5880, a double-sided laminate with PTFE fiberglass dielectric.

Since the patch antenna is assumed to be fixed on the target structure, only the cantilevered beam of the antenna node can move when a vibration is caused in the structure. The acceleration is regarded as uniform all over the cantilevered beam. During the simulation, a uniform body load defined by (9) is applied to the cantilevered beam to simulate the effect of vibration a defined by

$$q = a\rho \tag{19}$$

$$a = a_0 \sin 2\pi\omega t \tag{20}$$

where q is the body load, ρ is the density of the cantilevered beam, ω is the frequency, t is the time of the vibration,

Authorized licensed use limited to: TONGJI UNIVERSITY. Downloaded on June 05,2023 at 01:44:33 UTC from IEEE Xplore. Restrictions apply.

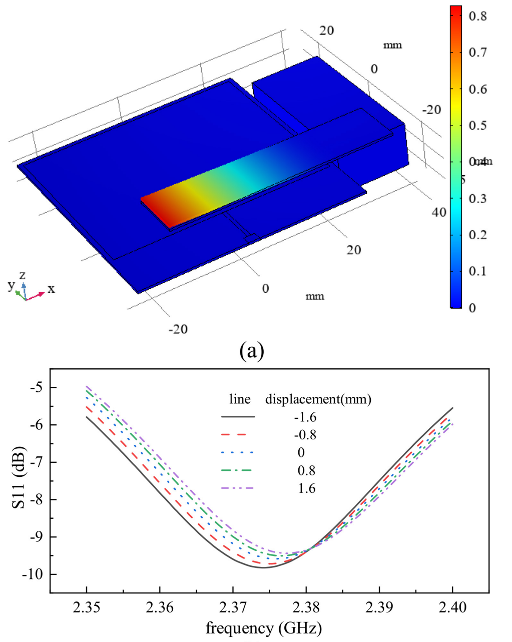

(a)

(b)

Fig. 13. Deformation and S_{11} curve of patch antenna. (a) Deformation. (b) S_{11}.

and a_0 is the maximum absolute value of acceleration. These parameters are also listed in Table I.

B. Resonant Frequency, Return Loss, and Displacement

First, the proposed antenna's resonant frequencies under five kinds of maximum displacements (1.6 mm, 0.8 mm, 0 mm, −0.8 mm, 1.6 mm), and the return loss are obtained and then utilized for calibration.

To ensure the ability of the sensing node, the resonant frequency, and return loss are calculated for the patch with different loads. First, the deformation and S_{11} curve under the five conditions mentioned in the first paragraph of this section is obtained and shown in Fig. 13. Then, the relationship between displacement, resonant frequency, and return loss is obtained from the corresponding S_{11} curves and is further illustrated in Fig. 14. The linear fitted line displayed in (21) is then calculated and selected as the transfer equation from resonant frequency f to the displacement d of the patch

$$f = 1.44y + 2376. \tag{21}$$

Then, the fitted line for the return curve S and displacement d is defined by (22). However, the exact value of the return loss is not credible, so the corresponding displacement of the return loss should be first identified by the resonant frequency as (17) and (18) shown

$$S = 0.124y - 9.613. \tag{22}$$

Equations (21) and (22) are the transform equations between the resonant frequency, return loss, and displacement. This simulation indicates a linear relationship between the return loss, resonant frequency, and displacement.

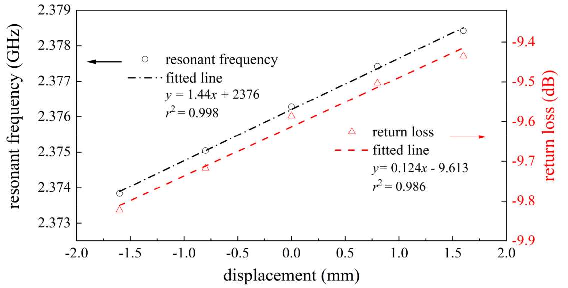

Fig. 14. Relationship between return loss, displacement, and resonant frequency.

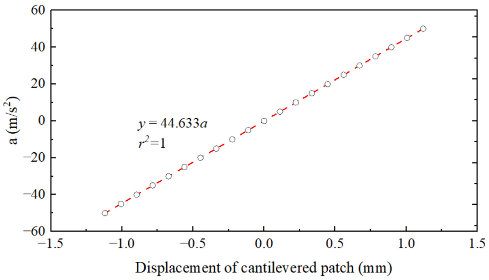

Fig. 15. Displacement under dead body load.

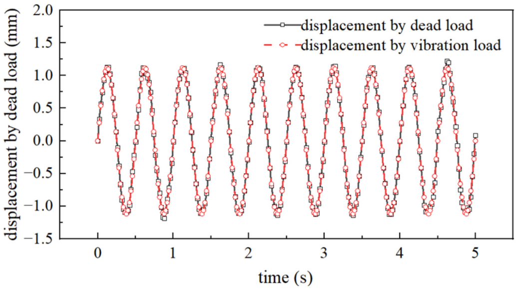

Fig. 16. Displacement caused by dead load and vibration load.

C. Input Acceleration and Displacement of Cantilevered Patch

After confirming the linearity between resonant factors and displacement, the relationship between displacement and acceleration is analyzed. First, assuming a dead body load, q, as defined by (19) is applied to the cantilevered patch. The corresponding maximum displacement of the patch y_s is shown in Fig. 15.

The fitting (23) for the maximum displacement and dead load will be selected for calibration

$$a_s = 44.633y_s. \tag{23}$$

Then, the attached structure is assumed to have a simple harmonic vibration defined by (20). The relationship between displacements caused by the dead load, y_s, and vibration load, y, is then shown in Fig. 16. These two displacements are nearly equal, as shown in (24)

$$y = y_s. \tag{24}$$

Based on these two displacements, the corresponding accelerations are obtained through (13) and (23), as shown in Fig. 17.

Authorized licensed use limited to: TONGJI UNIVERSITY. Downloaded on June 05,2023 at 01:44:33 UTC from IEEE Xplore. Restrictions apply.

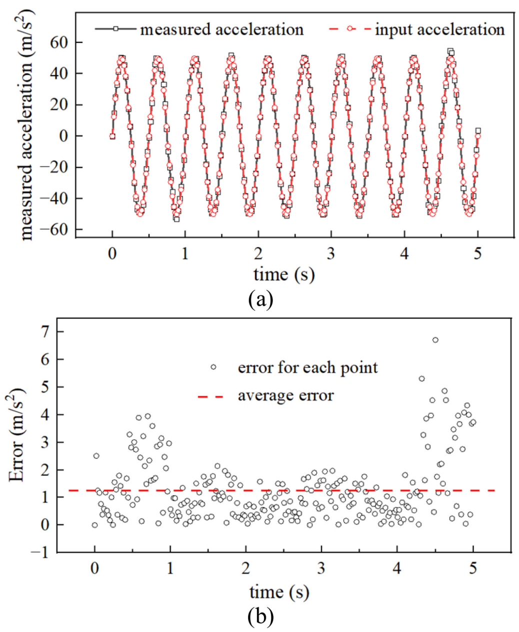

(a)

(b)

Fig. 17. Relationship between the acceleration of the target structure and displacement of the cantilevered patch. (a) Time domain. (b) Error.

Combining (21)–(24), the transform equation for resonant frequency, return loss, and acceleration are calculated as

$$f = 0.03226a + 2376. \quad (25)$$

$$S = 0.00278a - 9.613. \quad (26)$$

These two transformed equations indicate a linear relationship between the measuring parameters and acceleration. That is, the acceleration can be obtained by measuring real-time resonant frequency and return loss. However, since the feed line and lump port are utilized for interrogation instead of FMCW radar, the simulation did not consider the effect of transmission and diffusion in the free space. It can only show a brief working state for the proposed accelerometer. Hence, an experiment is still needed to further verify the workability, especially for interrogation.

IV. EXPERIMENT

Fig. 1 shows fabrication as containing three parts: 1) the antenna sensor (sensing node); 2) FMCW radar; and 3) the data collector. For the fabricated sensor, the substrate is made by Rogers RT/duroid 5880 with copper covered on both sides as the radiation patch and ground. The FMCW radar mainly consists of a VCO working in the bandwidth from 2.3 to 2.7 GHz for signal generation, an amplifier, and a planar ultra-wideband antenna for the signal emission. The oscilloscope is directly utilized as a data collector to simplify the experiment setting, which an analog can replace with a digital converter (ADC) for practical use.

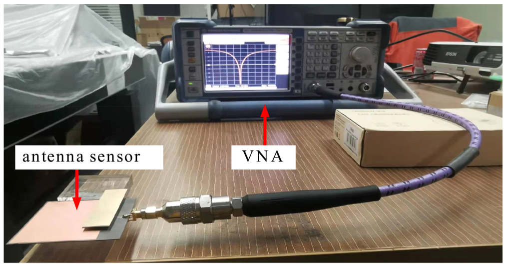

Fig. 18. Testing method for the calibration.

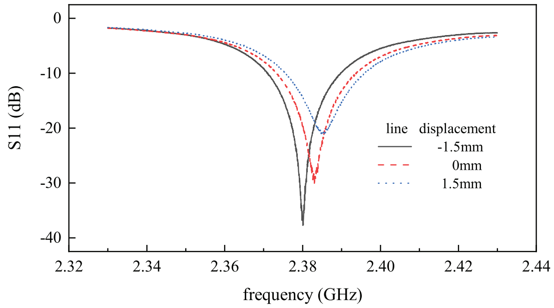

Fig. 19. S_{11} curve of antenna sensor during calibration.

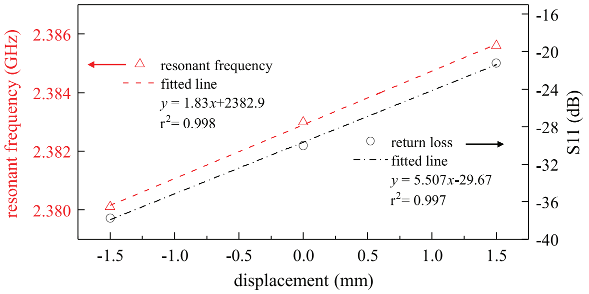

Fig. 20. Relationship between return loss, displacement, and resonant frequency.

A. Calibration of Patch Antenna Sensor

First, the displacement of the cantilevered patch is measured when the antenna sensor is set under the action of gravity, equaling 0.21 mm. This displacement is regarded as the drift response, y_s for a dead load equaling gravitational acceleration, which is utilized for calibration calculated as

$$a_s = 47.619 y_s. \quad (27)$$

Then, similar to the simulation mentioned at the beginning of this section, the resonant frequency and return loss of three states (initial state, maximum positive, and negative load) are obtained to calibrate the sensor. Since the force is hard to control as a constant state, the maximum displacement of the cantilevered beam is utilized as the control parameter for the calibration, as shown in Fig. 18. The maximum and minimum displacement are set at 1.5 mm, considering the displacement between the cantilevered beam and radiation patch. The S_{11} curves are tested by a VNA in this part of the experiment.

The S11 curves are plotted in Fig. 19, and the relationship between displacement, resonant frequency, and return loss are displayed in Fig. 20. Similar to the simulation, the resonant frequency and return loss will linearly increase with the displacement decrease. The linear fitting coefficients for these two relationships are higher than 0.99, indicating excellent workability for the proposed sensing node.

Authorized licensed use limited to: TONGJI UNIVERSITY. Downloaded on June 05,2023 at 01:44:33 UTC from IEEE Xplore. Restrictions apply.

TABLE II
CALIBRATION PARAMETER

Parameters	**Simulation**		**Experiment**	
	Resonant frequency (MHz/mm)	S_{11} (dB/mm)	Resonant frequency (MHz/mm)	S_{11} (dB/mm)
Sensitivity	1.44	0.13	1.8	5.5
Linear fitting coefficient (1)	0.986	0.998	0.998	0.997

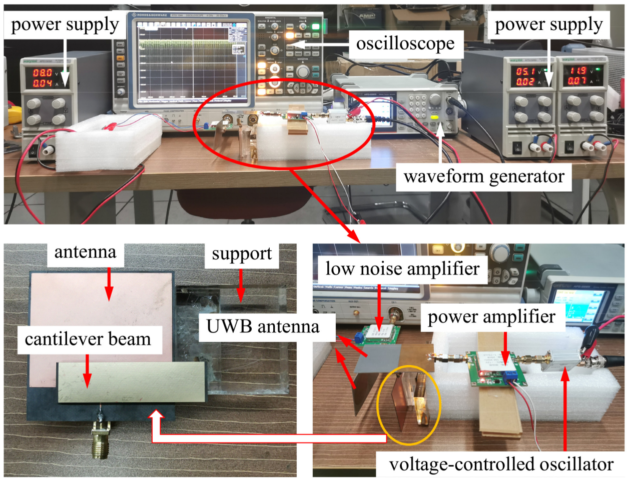

Fig. 21. Experiment setup.

The fitted (28) for the resonant frequency and displacement will be utilized to calibrate the testing data during the measurements. Since the return loss is a relative relationship, the fitting transfer equation should be determined with data from measuring resonant frequency and expressed as

$$f = 1.83x + 2382.9. \quad (28)$$

The sensitivity and linear fitting coefficient obtained from the simulation and experiment are then listed in Table II. Both the simulation and experiment have a linear fitting coefficient larger than 0.98, indicating great workability for the proposed sensor.

B. Experiment Setup

The testing device is established and displayed in Fig. 21. The antenna sensor, emitting antenna, and receiving antenna are fabricated in the lab. The emitting and receiving antenna is designed to be a wideband antenna to fit the working band of FMCW. First, the signal generator generates a sawtooth signal and then input for the VCO to obtain the FMCW. The FMCW is transmitted by the emitting antenna to the antenna sensor and then caught by the receiving antenna. Finally, the received signal is input into the oscilloscope and turned into a digital signal for data processing. Since the signal's power is insufficient for long-distance transmission in free space, the distance between the antenna sensor, emitting antenna, and receiving antenna is limited to 3 cm. The interrogation distance can be enlarged easily by improving the power amplifier set in this system.

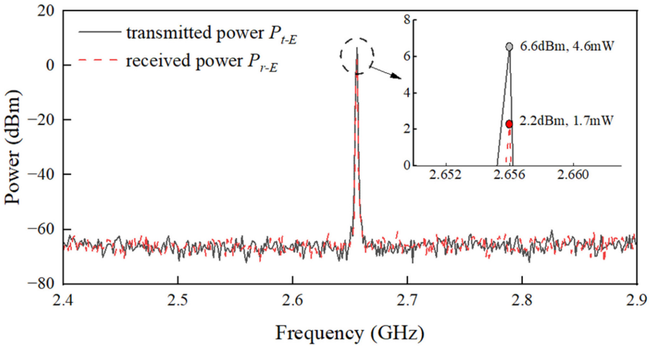

Fig. 22. Measured results using SA.

C. Analyzation of Power Transfer Efficiency

The power transfer efficiency (PTE) is first analyzed by the spectrum analyzer (SA). The transmitted power P_{t-E} and received power P_{r-E} are measured directly by connecting the VCO and received UWB antenna with the SA separately. During the measurement, the distance between the transmitting and receiving UWB antennas is 2 cm. Then, the peak value at the frequency domain for these two conditions is selected to calculate the PTE by (29). The result plotted in Fig. 22 shows a PTE of 36%, which is capable of the feasibility testing of the proposed acceleration sensing node. In the future, other energy harvesting methods can be applied to this node to improve wireless communication

$$\mathrm{PTE} = P_{r-E}/P_{t-E}. \quad (29)$$

D. Calculation of Dynamic Displacement

For the proposed sensing node, the acceleration measurement is realized by measuring the vibration of the cantilevered beam. Hence, the vibration of the cantilevered beam is tested to verify the workability of the proposed accelerometer.

Fig. 23(a) shows how the vibration is imposed by applying an initial positive displacement of 2.5 mm to the cantilevered beam in the horizontal direction. Regarding this movement as simple harmonic vibration, according to 32-time-lapse photography, the cantilevered beam shakes about 17 times in 0.25 s, and the amplitude decreases by half in the fourth round. Based on that, the period T, damping rate ξ, and frequency ω_f are calculated based on (30) and (31)

$$T = 2\pi/\omega_f = 0.25/17 = 0.0147\ (s) \quad (30)$$

$$e^{-4T\xi\frac{2\pi}{T}} = 0.5. \quad (31)$$

The basic parameters for the vibration are then solved and listed in Table III. Amplitude, A, is determined as 2.5 mm according to the initial setting.

Then, the expected displacement x(t) of the cantilevered beam under this free vibration is calculated using (32) and is plotted in Fig. 23(b)

$$x(t) = Ae^{-\xi\omega_f t}\cos\omega_f t. \quad (32)$$

The basic parameters of the FMCW radar are then listed in Table IV, where T_s is the sampling time for the radar, f_s is the repeated frequency of FMCW, which corresponds to

Authorized licensed use limited to: TONGJI UNIVERSITY. Downloaded on June 05,2023 at 01:44:33 UTC from IEEE Xplore. Restrictions apply.

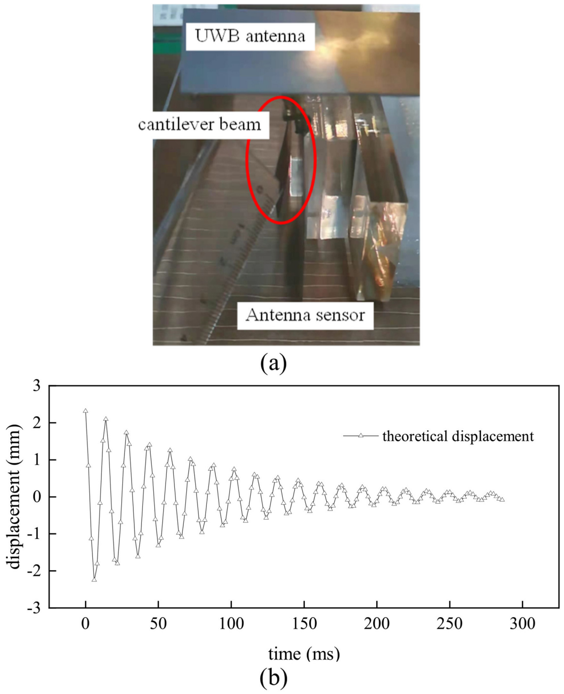

(a)

(b)

Fig. 23. Vibration of the cantilevered beam based on (a) setup and (b) free vibration.

TABLE III
BASIC PARAMETERS OF VIBRATION

Parameters	$\boldsymbol{T}$ (s)	ξ (1)	ω_f (1/s)	$\boldsymbol{A}$ (mm)
Value	0.0147	0.0276	427.43	2.5

TABLE IV
BASIC PARAMETERS OF FMCW RADAR

Parameters	T_s (s)	f_s (Hz)	f_{up} (GHz)	f_{up} (GHz)
Value	1	500	2.30	2.70

the sampling frequency of the system. f_{up} and f_{low} are the uplink and downlink frequency of FMCW, respectively, which corresponds to the interrogating range of the FMCW radar.

Then, the envelope diagram of the remaining FMCW signal is obtained by the oscilloscope and plotted in Fig. 24(a). The curves in Fig. 24(a) become smoother using average filtering, which are plotted in Fig. 24(b). The x label is changed from time to frequency based on the linear relationship. It is evident that the resonant point is contained in the band between 2.3 and 2.5 GHz. Hence, the data inside this frequency range is considered for the following data process. Here, the signal voltage is utilized to show the power.

Since the power of the initial signal in the frequency band is not flat, the received voltage signal should subtract the original one to get the needed variation during measurement. Since it is unrealistic to get a fundamental signal, all of them are subtracted from the signal with maximum voltage. The signal is then smoothed with a moving window containing 20 points and plotted in Fig. 25. Then, the resonant frequency of each time is obtained from the x coordinate of the average point, as Fig. 26 shows. After that, the received resonant frequency is applied to calculate the corresponding displacement based on the transfer (29). Compared with the expected free vibrations with the parameters shown in Table II, the result using resonant frequency is shown in Fig. 27.

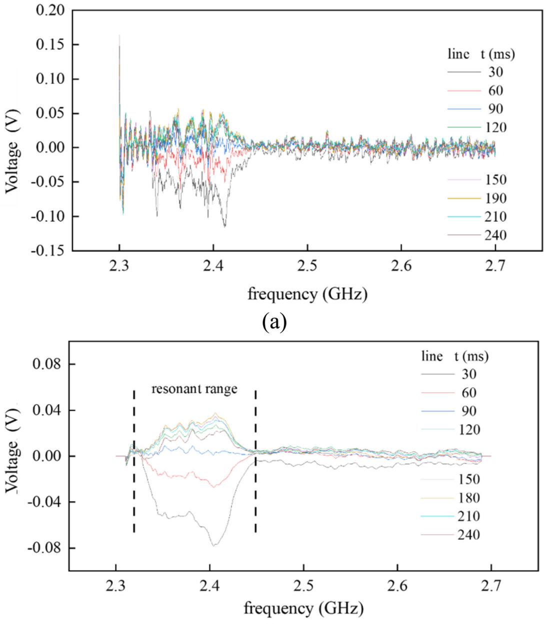

(a)

(b)

Fig. 24. Power of received signal. (a) Original. (b) After filtering.

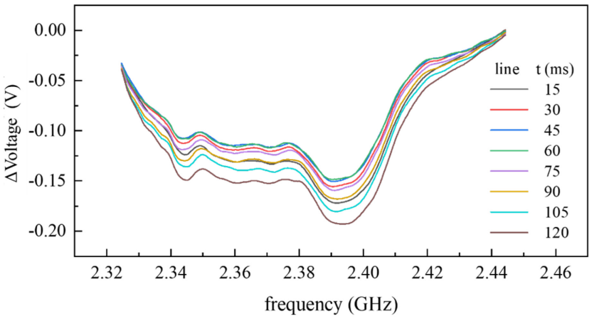

Fig. 25. Relationship between Δ Voltage (V) and resonant frequency (GHz).

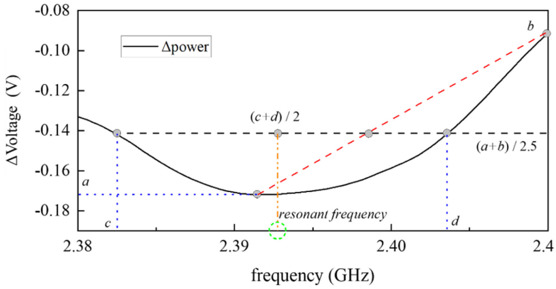

Fig. 26. Method to obtain the resonant frequency.

Then, based on the method proposed by (17) and (18), the relationship between the remaining power and displacement is shown in (33), which is then applied to the measured remaining powers to get the corresponding displacement, as shown in Fig. 28. Then, the error using the two methods is shown in Fig. 29

$$x = -21.457P + 0.1004. \tag{33}$$

Authorized licensed use limited to: TONGJI UNIVERSITY. Downloaded on June 05,2023 at 01:44:33 UTC from IEEE Xplore. Restrictions apply.

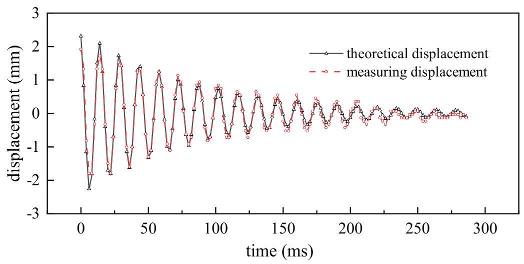

Fig. 27. Detected acceleration using obtained resonant frequency.

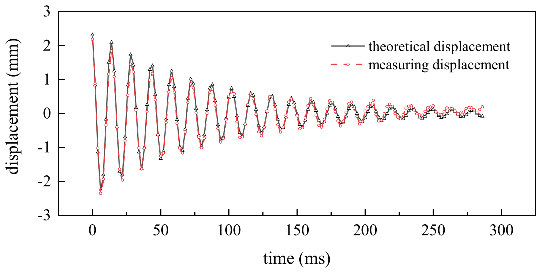

Fig. 28. Detected acceleration using obtained remaining power.

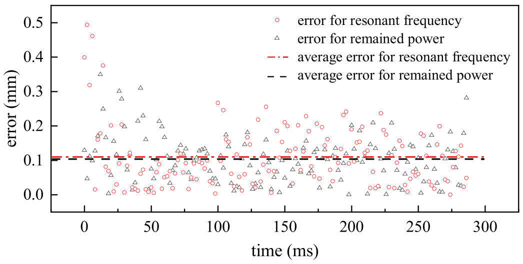

Fig. 29. Error of the proposed methods for vibrated displacement.

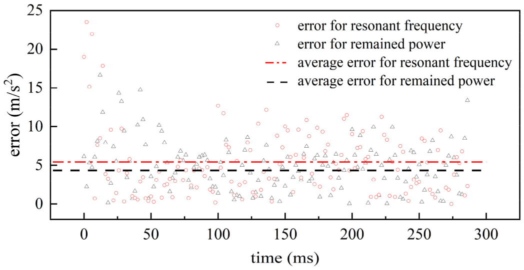

Fig. 30. Error of the proposed methods for acceleration.

The results in Figs. 27 and 28 show a great fit between the measuring data and theoretical data. The average errors for the whole test are 0.1028 and 0.1070 mm, corresponding to the results obtained from the resonant frequency and remaining power.

Despite the measurement for the vibrated displacement of the cantilevered patch, the measuring error when applied to the acceleration of the target structure can still be obtained by using (27), as shown in Fig. 30. The average errors are 4.89 and 5.09 m/s^2 for the results using the remaining power and resonant frequency. The corresponding measuring range for the displacement variation is ±110 m/s^2. Compared with the measuring range, this measuring error is within 4.5%, indicating a good workability of the proposed sensing method.

V. CONCLUSION

This article introduces a passive patch antenna sensing system for measuring the acceleration of the structure. The resonant frequency shift and the power change of a designed patch antenna sensing node can be utilized as sensing parameters for the displacement of the cantilevered beam in the node, which further reflects the acceleration of the attached structure. An equivalent model based on the structural dynamics and a simulated model in COMSOL Multiphysics is adopted to verify the design availability. The relationship between the antenna node's remaining power, resonant frequency, and structure acceleration are simulated and estimated as linear. To further verify the workability, an experiment was conducted to detect the displacement of the cantilevered beam in the sensing node. An FMCW radar frequency was designed corresponding to the basic parameters of the sensing node and then applied to the wireless measurement. The average error rate for the acceleration detection is within 4.5%, which corresponds to the measured data using resonant frequency and the remaining power, indicating excellent workability for the proposed sensing system.

In the next step, the calibration of the sensing system should be well-optimized. In addition, the sensing system is expected to be measured under a vibration load to verify its workability.

REFERENCES

[1] S. Xue, K. Xu, L. Xie, and G. Wan, "Crack sensor based on patch antenna fed by capacitive microstrip lines," *Smart Mater. Struct.*, vol. 28, no. 8, 2019, Art. no. 85012.

[2] T.-H. Yi, H.-B. Huang, and H.-N. Li, "Development of sensor validation methodologies for structural health monitoring: A comprehensive review," *Measurement*, vol. 109, pp. 200–214, Oct. 2017.

[3] D. Gao, Z. Wu, L. Yang, and Y. Zheng, "Integrated impedance and Lamb wave–based structural health monitoring strategy for long-term cycle-loaded composite structure," *Struct. Health Monit.*, vol. 17, no. 4, pp. 763–776, 2018.

[4] Y. Xia, P. Wang, and L. Sun, "Neutral axis-based health monitoring and condition assessment techniques for concrete box girder bridges," *Int. J. Struct. Stab. Dyn.*, vol. 19, no. 1, 2019, Art. no. 1940015.

[5] Z. Chen, H. Li, and Y. Bao, "Analyzing and modeling inter-sensor relationships for strain monitoring data and missing data imputation: A copula and functional data-analytic approach," *Struct. Health Monit.*, vol. 18, no. 4, pp. 1168–1188, 2019.

[6] T. Li, J. Guo, Y. Tan, and Z. Zhou, "Recent advances and tendency in fiber Bragg grating-based vibration sensor: A review," *IEEE Sensors J.*, vol. 20, no. 20, pp. 12074–12087, Oct. 2020.

[7] T. Loss, O. Gerler, and A. Bergmann, "Using MEMS acceleration sensors for monitoring blade tip movement of wind turbines," in *Proc. IEEE SENSORS*, 2018, pp. 1–4.

[8] H. Kataoka, Y. Kimura, H. Fujita, and S. Takatani, "Measurement of the rotor motion and corresponding hemolysis of a centrifugal blood pump with a magnetic and hydrodynamic hybrid bearing," *Artif. Organs*, vol. 29, no. 7, pp. 547–556, 2005.

[9] R. N. Nof, A. I. Chung, H. Rademacher, L. Dengler, and R. M. Allen, "MEMS accelerometer mini-array (MAMA): A low-cost implementation for earthquake early warning enhancement," *Earthq. Spectra*, vol. 35, no. 1, pp. 21–38, 2019.

[10] W. Huang, W. Zhang, B. Zhao, J. Zhang, and F. Li, "Earthquake response monitoring of high-rise building using fiber optic accelerometers," in *Proc. Opt. Fibers Fiber-Based Devices Appl.*, 2019, p. OFTu3A-6.

[11] S. Mustafa, H. Sekiya, S. Hirano, and C. Miki, "Iterative linear optimization method for bridge weigh-in-motion systems using accelerometers," *Struct. Infrastruct. Eng.*, vol. 17, no. 9, pp. 1245–1256, 2021.

[12] A. Mustafazade et al., "A vibrating beam MEMS accelerometer for gravity and seismic measurements," *Sci. Rep.*, vol. 10, no. 1, pp. 1–8, 2020.

Authorized licensed use limited to: TONGJI UNIVERSITY. Downloaded on June 05,2023 at 01:44:33 UTC from IEEE Xplore. Restrictions apply.

[13] J. Sun et al., "Design and performance study on a new biaxial micro-accelerometer with variable cross-section beam," *Microsyst. Technol.*, vol. 27, no. 11, pp. 4111–4120, 2021.

[14] X. Wang, Y. Guo, L. Xiong, and H. Wu, "High-frequency optical fiber Bragg grating accelerometer," *IEEE Sensors J.*, vol. 18, no. 12, pp. 4954–4960, Jun. 2018.

[15] R. Mukhiya et al., "Design, modelling and system level simulations of DRIE-based MEMS differential capacitive accelerometer," *Microsyst. Technol.*, vol. 25, no. 9, pp. 3521–3532, 2019.

[16] A. L. Gesing, F. D. P. Alves, S. Paul, and J. A. Cordioli, "On the design of a MEMS piezoelectric accelerometer coupled to the middle ear as an implantable sensor for hearing devices," *Sci. Rep.*, vol. 8, no. 1, pp. 1–10, 2018.

[17] C. Wan, Z. Zheng, S. Xue, X. I. E. Liyu, and G. Wan, "An angle sensor based on a sector ring patch antenna for bolt loosening detection," *Smart Mater. Struct.*, vol. 31, Feb. 2022, Art. no. 45009.

[18] L.-S. Liu, J.-Q. Ni, R.-Q. Zhao, M.-X. Shen, C.-L. He, and M.-Z. Lu, "Design and test of a low-power acceleration sensor with Bluetooth low energy on ear tags for sow behaviour monitoring," *Biosyst. Eng.*, vol. 176, pp. 162–171, Dec. 2018.

[19] T. Torfs et al., "Low power wireless sensor network for building monitoring," *IEEE Sensors J.*, vol. 13, no. 3, pp. 909–915, Mar. 2013.

[20] A. Sabato, C. Niezrecki, and G. Fortino, "Wireless MEMS-based accelerometer sensor boards for structural vibration monitoring: A review," *IEEE Sensors J.*, vol. 17, no. 2, pp. 226–235, Jan. 2017.

[21] L. Zhu, Y. Fu, R. Chow, B. F. Spencer Jr., J. W. Park, and K. Mechitov, "Development of a high-sensitivity wireless accelerometer for structural health monitoring," *Sensors*, vol. 18, no. 1, p. 262, 2018.

[22] Z. Shen, C. Y. Tan, K. Yao, L. Zhang, and Y. F. Chen, "A miniaturized wireless accelerometer with micromachined piezoelectric sensing element," *Sens. Actuat. A, Phys.*, vol. 241, pp. 113–119, Apr. 2016.

[23] B. F. Spencer, T. Hoang, and K. A. Mechitov, "Energy-efficient autonomous framework for monitoring railroad bridges in the USA using wireless smart sensors," in *Bridge Maintenance, Safety, Management, Life-Cycle Sustainability and Innovations*. Boca Raton, FL, USA: CRC Press, 2021, pp. 91–99.

[24] S. A. V. Shajihan, R. Chow, K. Mechitov, Y. Fu, T. Hoang, and B. F. Spencer Jr., "Development of synchronized high-sensitivity wireless accelerometer for structural health monitoring," *Sensors*, vol. 20, no. 15, p. 4169, 2020.

[25] Y. Fu, C. Peng, F. Gomez, Y. Narazaki, and B. F. Spencer Jr., "Sensor fault management techniques for wireless smart sensor networks in structural health monitoring," *Struct. Control Health Monit.*, vol. 26, no. 7, p. e2362, 2019.

[26] L. He and B. Sun, "Exploring the EPR system for power battery recycling from a supply-side perspective: An evolutionary game analysis," *Waste Manag.*, vol. 140, pp. 204–212, Mar. 2022.

[27] M. S. Khan, M. Javed, M. T. Rehman, M. Urooj, and M. I. Ahmad, "Heavy metal pollution and risk assessment by the battery of toxicity tests," *Sci. Rep.*, vol. 10, no. 1, pp. 1–10, 2020.

[28] S.-Y. Wu, C.-Y. Hung, and W. Hsu, "A wirelessly readable and resettable shock recorder through the integration of LC circuits and MEMS devices," *Smart Mater. Struct.*, vol. 23, no. 9, 2014, Art. no. 95030.

[29] P. Schmitt and M. Hoffmann, "A passive acceleration sensor with mechanical 6 bit memory and mechanical analog-to-digital converter," *Micro Nano Eng.*, vol. 15, Jun. 2022, Art. no. 100142.

[30] J. D. Tanner and B. D. Jensen, "Power-free bistable threshold accelerometer made from a carbon nanotube framework," *Mech. Sci.*, vol. 4, no. 2, pp. 397–405, 2013.

[31] W. C. Wilson, J. P. Moore, and K. R. Brinker, "The use of a reflectometer as a monostatic radar for measuring aircraft structural flutter," in *Proc. IEEE Nat. Aerosp. Electron. Conf. (NAECON)*, 2019, pp. 702–706.

[32] W. C. Wilson and J. P. Moore, "Passive wireless vibration sensing for measuring aerospace structural flutter," in *Proc. IEEE Int. Conf. Wireless Space Extreme Environ. (WiSEE)*, 2017, Art. no. NF1676L-27677.

[33] G. C. Wan, M. M. Li, Y. L. Yang, L. Xie, and L. Chen, "Patch-antenna-based structural strain measurement using optimized energy detection algorithm applied on USRP," *IEEE Internet Things J.*, vol. 8, no. 9, pp. 7476–7484, May 2021.

[34] S. Xue, Z. Yi, L. Xie, and G. Wan, "Double-frequency passive deformation sensor based on two-layer patch antenna," *Smart Struct. Syst.*, vol. 27, no. 6, pp. 969–982, 2021.

[35] K. M. Labus, B. M. Notaroš, M. M. Ilić, C. J. Sutherland, A. Holcomb, and C. M. Puttlitz, "A coaxial dipole antenna for passively sensing object displacement and deflection for orthopaedic applications," *IEEE Access*, vol. 6, pp. 68184–68194, 2018.

[36] K. L. Chung, L. Wang, J. Luo, Y. Li, and Y. Li, "Comparative study on directional sensitivity of patch-antenna-based strain sensors," *Int. J. RF Microw. Comput.-Aided Eng.*, vol. 30, no. 11, 2020, Art. no. e22398.

[37] M. Bhattacharjee, F. Nikbakhtnasrabadi, and R. Dahiya, "Printed chipless antenna as flexible temperature sensor," *IEEE Internet Things J.*, vol. 8, no. 6, pp. 5101–5110, Mar. 2021.

[38] J. Zhang, B. Huang, G. Zhang, and G. Y. Tian, "Wireless passive ultra high frequency RFID antenna sensor for surface crack monitoring and quantitative analysis," *Sensors*, vol. 18, no. 7, p. 2130, 2018.

[39] X. Li, S. Xue, L. Xie, G. Wan, and C. Wan, "An off-center fed patch antenna with overlapping sub-patch for simultaneous crack and temperature sensing," *Smart Mater. Struct.*, vol. 31, no. 9, 2022, Art. no. 95036.

[40] K. Jiang, L. Xie, S. Xue, and G. Wan, "Capacitively-coupled dual ring antennas for bolt loosening detection," *Measurement*, vol. 200, Aug. 2022, Art. no. 111605.

[41] S. Xue, X. Li, L. Xie, Z. Yi, and G. Wan, "A bolt loosening detection method based on patch antenna with overlapping sub-patch," *Struct. Health Monit.*, vol. 21, no. 5, pp. 2231–2243, 2022.

[42] S. Xue, Z. Yi, L. Xie, G. Wan, and T. Ding, "A displacement sensor based on a normal mode helical antenna," *Sensors*, vol. 19, no. 17, p. 3767, 2019.

[43] J. Yao, F. M. Tchafa, A. Jain, S. Tjuatja, and H. Huang, "Far-field interrogation of microstrip patch antenna for temperature sensing without electronics," *IEEE Sensors J.*, vol. 16, no. 19, pp. 7053–7060, Oct. 2016.

[44] H. Huang, "Antenna sensors in passive wireless sensing systems," in *Handbook of Antenna Technologies*. Singapore: Springer, 2016, pp. 2795–2838.

[45] J. Yao, J. Skilskyj, and H. Huang, "A compact, low-cost, real-time interrogation system for dynamic interrogation of microstrip patch antenna sensor," in *Proc. Sens. Smart Struct. Technol. Civil Mech. Aerosp. Syst.*, 2018, pp. 238–244.

[46] S. Farhangdoust, G. Georgeson, J.-B. Ihn, and F.-K. Chang, "Kirigami auxetic structure for high efficiency power harvesting in self-powered and wireless structural health monitoring systems," *Smart Mater. Struct.*, vol. 30, no. 1, 2020, Art. no. 15037.

[47] Y. Alazzawi, K. Aono, E. L. Scheller, and S. Chakrabartty, "Exploiting self-capacitances for wireless power transfer," *IEEE Trans. Biomed. Circuits Syst.*, vol. 13, no. 2, pp. 425–434, Apr. 2019.

[48] X. Gao, H. Zhou, W. Hu, Q. Deng, G.-P. Liu, and J. Lai, "Capacitive power transfer through virtual self-capacitance route," *IET Power Electron.*, vol. 11, no. 6, pp. 1110–1118, 2018.

[49] Z. Liu, Y. Su, H. Hu, Z. Deng, and R. Deng, "Research on transfer mechanism and power improvement technology of the SCC-WPT system," *IEEE Trans. Power Electron.*, vol. 38, no. 1, pp. 1324–1335, Jan. 2023.

[50] A. M. Jawad, R. Nordin, S. K. Gharghan, H. M. Jawad, and M. Ismail, "Opportunities and challenges for near-field wireless power transfer: A review," *Energies*, vol. 10, no. 7, p. 1022, 2017.

[51] M. Song et al., "Wireless power transfer based on novel physical concepts," *Nat. Electron.*, vol. 4, no. 10, pp. 707–716, 2021.

[52] S. R. Khan, S. K. Pavuluri, G. Cummins, and M. P. Y. Desmulliez, "Wireless power transfer techniques for implantable medical devices: A review," *Sensors*, vol. 20, no. 12, p. 3487, 2020.

[53] J. Yao, S. Tjuatja, and H. Huang, "Real-time vibratory strain sensing using passive wireless antenna sensor," *IEEE Sensors J.*, vol. 15, no. 8, pp. 4338–4345, Aug. 2015.

[54] J. Humar, *Dynamics of Structures*. Boca Raton, FL, USA: CRC Press, 2012.

Zhuoran Yi received the B.S. and M.S. degrees in civil engineering from Tongji University, Shanghai, China, in 2018 and 2021.

His current research interests focus on the smart sensors for the structural health monitoring and FMCW-based radio frequency identification detection systems.

Authorized licensed use limited to: TONGJI UNIVERSITY. Downloaded on June 05,2023 at 01:44:33 UTC from IEEE Xplore. Restrictions apply.

Liyu Xie (Member, IEEE) received the B.S. and M.S. degrees in mechanics engineering from Tongji University, Shanghai, China, in 2000 and 2003, respectively, and the Ph.D. degree in system design engineering from Keio University, Tokyo, Japan, in 2009.

Since 2009, he has been with the College of Civil Engineering, Tongji University, where he is currently an Associator Professor. His current research focuses on smart sensors, structural health monitoring, and structural vibration control.

Songtao Xue received the B.S. degree in mechanics engineering from Tongji University, Shanghai, China, in 1985, and the M.S. and Ph.D. degrees in structural engineering from Tohoku University, Sendai, Japan, in 1989 and 1991, respectively.

From 1991, he was as an Assistant Professor with the Department of Architecture, Tohoku University and then was promoted to an Associate Professor in 1995. Since 1996, he joined Tongji University, where he is a Full Professor until now. From 2010, he joined the Department of Architecture, Tohoku Institute of Technology, where he is currently the Director with the Department of Architecture. His research focuses on structural health monitoring, seismic engineering, and structural vibration control.

Guochun Wan (Member, IEEE) received the M.S. and Ph.D. degrees in transportation information engineering and control from Tongji University, Shanghai, China, in 2005 and 2011, respectively.

He became an Associate Professor with Tongji University in 2002. He joined the Department of Electronic Science and Technology, Tongji University, in 2006. His current research interests include signal and information processing, with an emphasis on error-correcting coding, VLSI architectures, RFID strain sensor, and System-on-Chip design for communications and coding theory applications.

Authorized licensed use limited to: TONGJI UNIVERSITY. Downloaded on June 05,2023 at 01:44:33 UTC from IEEE Xplore. Restrictions apply.